HHS Public Access

Author manuscript

Nat Genet. Author manuscript; available in PMC 2017 October 01.

Published in final edited form as:

Nat Genet. 2017 April ; 49(4): 527–536. doi:10.1038/ng.3808.

Disruption of the ATXN1-CIC complex causes a spectrum of neurobehavioral phenotypes in mice and humans

Hsiang-Chih Lu[1,2,†,*], **Qiumin Tan**[2,3,*], **Maxime WC Rousseaux**[2,3], **Wei Wang**[2,3], **Ji-Yoen Kim**[2,3], **Ronald Richman**[2,3,4], **Ying-Wooi Wan**[2,3], **Szu-Ying Yeh**[1,2], **Jay M Patel**[5], **Xiuyun Liu**[2,3,4], **Tao Lin**[2,6], **Yoontae Lee**[2,3,††], **John D Fryer**[2,3,‡], **Jing Han**[2,3,‡‡], **Maria Chahrour**[3,§], **Richard H Finnell**[7], **Yunping Lei**[7], **Maria E Zurita-Jimenez**[7], **Priyanka Ahimaz**[8], **Kwame Anyane-Yeboa**[8], **Lionel Van Maldergem**[9], **Daphne Lehalle**[10,11,12], **Nolwenn Jean-Marcais**[10,11,12,13], **Anne-Laure Mosca-Boidron**[10,11,12,13], **Julien Thevenon**[10,11,12], **Margot A Cousin**[14,15], **Della E Bro**[14,16,§§], **Brendan C Lanpher**[14,16], **Eric W Klee**[14,15,16], **Nora Alexander**[17], **Matthew N Bainbridge**[3,18,19], **Harry T Orr**[20,21], **Roy V Sillitoe**[1,2,5,6], **M. Cecilia Ljungberg**[2,22], **Zhandong Liu**[2,22], **Christian P Schaaf**[2,3,23], and **Huda Y Zoghbi**[1,2,3,4,5,22,#]

[1]Program in Developmental Biology, Baylor College of Medicine, Houston, Texas, USA

[2]Jan and Dan Duncan Neurological Research Institute at Texas Children's Hospital, Houston, Texas, USA

[3]Department of Molecular and Human Genetics, Baylor College of Medicine, Houston, Texas, USA

[4]Howard Hughes Medical Institute, Baylor College of Medicine, Houston, Texas, USA

[5]Department of Neuroscience, Baylor College of Medicine, Houston, Texas, USA

[6]Department of Pathology and Immunology, Baylor College of Medicine, Houston, Texas, USA

[7]Department of Pediatrics, Dell Pediatric Research Institute, The University of Texas at Austin Dell Medical School, Austin, Texas, USA

[#]Correspondence should be addressed to H.Y.Z. (hzoghbi@bcm.edu).
[†]Present address: Department of Pathology and Immunology, Washington University School of Medicine, St. Louis, Missouri, USA.
[††]Present address: Department of Life Science, Pohang University of Science and Technology, Pohang, Kyungbuk, South Korea.
[‡]Present address: Department of Neuroscience, Mayo Clinic, Jacksonville, Florida, USA.
[‡‡]Present address: Institute for Applied Cancer Science, MD Anderson Cancer Center, Houston, Texas, USA.
[§]Present address: Eugene McDermott Center for Human Growth & Development, Neuroscience, Psychiatry, University of Texas Southwestern Medical Center, Dallas, Texas, USA.
[§§]Present address: Virginia Piper Cancer Institute, Allina Health, Minneapolis, Minnesota, USA.
[*]Co-first authors.

Data Availability

The gene expression data that support the findings of this study are available in the GEO (Gene Expression Omnibus) repository with the accession code GSE83243.

Author Contributions

H.L., Q.T., and H.Y.Z. conceived and designed the experiments. H.T.O. and R.V.S. provided critical input to the project. H.L., Q.T., M.WC.R., W.W., J.K., R.R., S.Y., J.M.P., T.L., and M.C.L. performed the experiments. X.L., Y.L., J.D.F., J.H., and M.C. assisted in generating the mouse models. Y.W. and Z.L. performed RNAseq analysis. M.E.Z.J. cultured fibroblasts for patient 1. Q.T. performed human fibroblast RNA and protein analysis. H.L., Q.T., R.H.F., Y.L., P.A., K.A-Y., L.V.M., D.L., N.J-M., A-L.M-B., J.T., M.A.C., D.B., B.L., E.W.K., N.A., M.N.B., C.P.S., and H.Y.Z. recruited patients, acquired clinical data, or analyzed whole-exome or Sanger sequencing results. H.L., Q.T., and H.Y.Z. drafted the original manuscript, and all authors assisted in editing the manuscript.

Competing Financial Interests

None declared.

[8]Department of Pediatrics, Columbia University Medical Center, New York, New York, USA

[9]Centre for Human Genetics, University of Franche-Comté, Besançon, France

[10]University Hospital Federation, Translational Medicine for Congenital Anomalies (TRANSLAD), Dijon University Hospital, F-21079 Dijon, France

[11]Genetic Center and Reference Center for Congenital Anomalies of the Est of France, Dijon University Hospital, F-21079 Dijon, France

[12]Research Unit 4271, Genetics for Congenital Anomalies, Burgundy University, F-1079 Dijon, France

[13]Chromosomal and Molecular Genetics Laboratory, Biological Center, Dijon University Hospital, F-21079 Dijon, France

[14]Center for Individualized Medicine, Mayo Clinic, Rochester, Minnesota, USA

[15]Department of Health Sciences Research, Mayo Clinic, Rochester, Minnesota, USA

[16]Department of Clinical Genomics, Mayo Clinic, Rochester, Minnesota, USA

[17]GeneDx, Gaithersburg, Maryland, USA

[18]Human Genome Sequencing Center, Baylor College of Medicine, Houston, Texas, USA

[19]Codified Genomics, LLC, Houston, Texas, USA

[20]Institute for Translational Neuroscience, University of Minnesota, Minneapolis, Minnesota, USA

[21]Department of Laboratory Medicine and Pathology, University of Minnesota, Minneapolis, Minnesota, USA

[22]Department of Pediatrics, Baylor College of Medicine, Houston, Texas, USA

[23]Texas Children's Hospital, Houston, Texas, USA

Abstract

Gain-of function mutations in some genes underlie neurodegenerative conditions whereas loss-of-function mutations have distinct phenotypes. Such appears to be the case with the protein ataxin 1 (ATXN1), which forms a transcriptional repressor complex with capicua (CIC). Gain-of-function of the complex leads to neurodegeneration, but ATXIN1-CIC is also essential for survival. We set out to understand the functions of ATXN1-CIC in the developing forebrain and found that losing the complex results in hyperactivity, impaired learning and memory, and abnormal maturation and maintenance of upper layer cortical neurons. We also found that CIC modulates social interactions in the hypothalamus and medial amygdala. Informed by these neurobehavioral features in mouse mutants, we identified five patients with *de novo* heterozygous truncating mutations in *CIC* that share similar clinical features, including intellectual disability, attention deficit/hyperactivity disorder (ADHD), and autism spectrum disorder. Our study demonstrates that loss of ATXN1-CIC complexes causes a spectrum of neurobehavioral phenotypes.

Introduction

Ataxin 1 (ATXN1) has been slow to yield its functions to investigation. Expansion of its polyglutamine tract was discovered in 1993 to produce the adult-onset disease spinocerebellar ataxia type 1, but deletion of the gene in *Atxn1*$^{-/-}$ mice produces only mild defects in learning and memory without neurodegeneration[1–5]. We subsequently discovered that mutant ataxin 1 alters transcription[6], and we searched for protein interactors that contribute to its activities. We found that the transcriptional repressor capicua (CIC) forms a co-repressor complex (ATXN1-CIC) *in vivo* with ATXN1 and with its paralog ataxin 1-like (ATXN1L), and that CIC anchors the complex to DNA to repress the target genes of CIC[7–9].

While these studies provided insights into ATXN1-CIC function, the consequences of losing ATXN1-CIC in the developing brain remains unknown. In mice, the ATXN1-CIC complex is essential for survival, as mice either lacking both *Atxn1* and *Atxn1l* or homozygous knockout allele of *Cic* that reduces CIC levels by more than 80% (*Cic-L)* die shortly after birth[9,10]. *Atxn1*$^{-/-}$*; Atxn1l*$^{-/-}$ mice exhibit hydrocephalus, abdominal wall closure defect, and lung defects[9]. *Cic-L*$^{-/-}$ mice phenocopy *Atxn1*$^{-/-}$*; Atxn1l*$^{-/-}$ mice, confirming that these three proteins indeed function as a complex *in vivo*[9]. Interestingly, large deletions spanning *ATXN1* on chromosome 6p22 have been reported in patients with autism spectrum disorder (ASD), developmental delay/intellectual disability (DD/ID), seizures, and attention deficit/hyperactivity disorder (ADHD)[11–13], but it is unclear whether the heterozygous loss of *ATXN1* or other genes in the deleted region lead to the clinical presentation. In the case of *CIC*, two different missense mutations have been reported in two isolated cases of intellectual disability[14,15], but here again it is unclear whether these variants are causative, because there have been no functional studies to confirm the pathogenicity of the reported missense variants in *CIC*.

We set out to investigate the neurodevelopmental consequences of losing the ATXN1-CIC complex. To bypass the early lethality caused by defects in peripheral organs[9], we utilized Cre-*loxP* technology to generate conditional knockouts of either *Atxn1-Atxn1l* or *Cic*. We first focused our study on the developing forebrain, a region known to contribute prominently to the clinical symptoms of patients with neurodevelopmental disorders[16,17], using *Emx1-Cre*[18]. We discovered that forebrain deletion of ATXN1-CIC caused learning/memory deficits and hyperactivity that responded to low-dose amphetamine. *Emx1-Cre* conditional mutant neurons exhibited histological and cellular defects. Loss of ATXN1-CIC complex outside of *Emx1-Cre* domains using *Otp-Cre*, which was expressed in the hypothalamus and medial amygdala, led to social interaction defects. Informed by the behavioral phenotypes, we searched for patients that have truncating mutations in *CIC*. We found five patients with *de novo* heterozygous truncating mutations in *CIC* that are predicted to undergo nonsense-mediated decay. These patients present with ASD, DD/ID, seizures, and ADHD, features overlapping with those uncovered by the mouse studies. Altogether these results demonstrate the necessity of ATXN1-CIC complex for normal brain development and reveal the region-specific contributions of dysfunctional ATXN1-CIC complex to intellectual disability, hyperactivity, and social behavioral deficits.

Results

Deleting the ATXN1-CIC complex in the developing forebrain results in multiple behavioral abnormalities

The stable ATXN1-CIC complex is present in many brain regions, including the cerebellum[7,8], cortex and hypothalamus (Supplementary Fig. 1). Because constitutive knockouts were not viable, we first utilized *Cic*$^{+/-}$ mice for our initial effort to study the roles of ATXN1-CIC complex in the brain. A battery of behavioral tests showed that *Cic*$^{+/-}$ mice behaved similarly to their wildtype littermate controls in all the tests except for the open field assay, where they exhibited mild hyperactivity (Supplementary Fig. 2). To further study the functions of the ATXN1-CIC complex in the developing brain, we generated conditional knockouts of either *Atxn1-Atxn1l* or *Cic* in the developing forebrain through breeding with *Emx1-Cre* mice, in which the Cre recombinase is expressed in progenitor cells in the dorsal telencephalon starting at embryonic day 10.5 (E10.5), and will delete the conditional alleles in forebrain excitatory neurons and glia[18]. We confirmed the knockout efficiency in the mutant mice by western blot and immunofluorescent staining, which demonstrated marked reduction of either ATXN1L or CIC protein levels (Supplementary Fig. 3a–c). Upregulation of the known CIC target genes *Etv1*, *Etv4* and *Etv5* in the mutant cortex further demonstrated efficient removal of the complex (Supplementary Fig. 3d).

We performed a series of behavioral tests on the *Atxn1-Atxn1l* and *Cic* conditional knockout mice to assess general activity, anxiety, learning/memory, and social behavior. Both mouse lines covered greater distance at greater speed in the open-field test than their littermate controls (Fig. 1a, b). Given the ADHD symptoms in patients with deletions spanning *ATXN1*[11], we tested the effects of low-dose amphetamine on the mutant mice. As has been shown in some ADHD models, low-dose amphetamine exerted a paradoxical calming effect on the mutant animals[19]. *Emx1-Cre; Cic*$^{flox/flox}$ groups treated with vehicle or amphetamine exhibited different baseline activities before the drug injection (time points 10–30 mins). We reasoned that this was probably due to chance and expected normal variability as the experimenters were blinded to the genotypes and treatments. Importantly, we found a significant interaction between genotype and drug (Fig. 1c, right panel), demonstrating the paradoxical calming effect of low-dose amphetamine on mutant mice. In the elevated plus-maze test, conditional knockout mice spent more time in the open-arm and less time in the closed-arm, which could be due to reduced anxiety (Fig. 1d, e). We used the fear conditioning assay to examine learning and memory in the conditional mutants, and discovered that they exhibited reduced freezing, especially in the test of spatial context, indicating that they have impaired learning and memory (Fig. 1f, g). Finally, we assessed social interaction behavior using the three-chamber test and found that the mutant mice behaved in a similar way to the control mice. (Supplemental Fig. 4).

It is worth noting that conditional knockouts of either *Atxn1-Atxn1l* or *Cic* displayed similar behavioral deficits, which is consistent with their role as constituents of a protein complex[9]. Interestingly, the protein levels of CIC were significantly reduced in the *Atxn1-Atxn1l* conditional knockout tissue, but the levels of ATXN1 and ATXN1L were not reduced in the

Cic conditional knockouts (Supplementary Fig. 3a, b), suggesting that the observed mutant phenotypes are mostly driven by the loss of CIC functions and disruption of the complex.

Deleting the ATXN1-CIC complex causes a postnatal reduction in the cortical thickness and the number of CUX1$^+$ cells

To determine whether the behavioral deficits in the mutant mice arise from abnormal anatomical development, we examined brain sections from 5-week old mice. We found that the structures of amygdala and hippocampus were similar between control and *Emx1-Cre* conditional knockout animals (Supplementary Fig. 5 and 6). The conditional knockout mice, however, had reduced thickness of cortical layer 2–4, while the thickness of layer 5–6 remained normal (Fig. 2a, b). At 20 weeks of age, the structures of amygdala remained comparable between control and mutant mice (Supplementary Fig. 7a and b). We observed a similar reduction in the thickness of cortical layer 2–4 in the mutants, whereas the thickness of layer 5–6 was not affected (Supplementary Fig. 7c). The hippocampal dentate gyrus from 20-week-old mutant mice showed decreased thickness, while the thickness of CA1 and CA3 regions were normal (Supplementary Fig. 7d). The dentate gyrus is critical for receiving and processing neuronal input from other brain regions, such as the entorhinal cortex, before sending signals to CA3[20]. The pathology in the dentate gyrus, which manifested when the mutant mice were older, might contribute to the learning and memory deficits in the contextual fear conditioning test (Fig. 1f, g). We further examined the synaptic plasticity in the hippocampus and found that, while basal synaptic transmission and long-term synaptic plasticity were preserved in the *Emx1-Cre Cic* knockout mice, there was a decrease in the probability of presynaptic neurotransmitter release (Supplementary Fig. 8).

We next examined the cortex using markers specific to layer 2–4 (CUX1), layer 5–6 (CTIP2, also known as BCL11B), and layer 2–6 (SATB2). Consistent with the Nissl staining results, the number of CTIP2$^+$ cells remained unchanged (Fig. 2c, d). Interestingly, while the number of SATB2$^+$ neurons in layer 2–4 was only slightly reduced, the number of layer 2–4 CUX1$^+$ neurons was dramatically reduced in the mutants (Fig. 2c, d). In control layer 2–4 neurons, most of the SATB2$^+$ cells co-expressed CUX1, in contrast to the mutants where only half of layer 2–4 SATB2$^+$ cells were CUX1-positive (Fig. 2d). These findings suggest that the reduction in CUX1$^+$ cells was primarily driven by the loss of CUX1 expression in layer 2–4 neurons. In support of this, *Cux1* expression was reduced in the mutant cortex (Supplementary Fig. 9a). The expression levels of *Cux2*, which is a paralog of *Cux1* and a marker for layer 2–4 pyramidal neurons, was however unaffected in the mutant cortex, suggesting there is no global defect in the fate of layer 2–4 neurons (Supplementary Fig. 9b). Because the majority of the callosal projection neurons (CPNs) reside in the upper cortical layers, and the projections of CPN form the corpus callosum[21], we examined the formation of the corpus callosum with Luxol Fast Blue staining, which stains myelin. The formation of the corpus callosum in the mutant brains was not disrupted, nor was the thickness of the corpus callosum significantly altered (Supplementary Fig. 10). Since *Atxn1-Atxn1l* conditional mutants phenocopied *Cic* conditional mutants, we next focused on *Cic* conditional mutants to further dissect the cortical defects resulting from the loss of function of the complex.

One possible explanation for the observed reduction in the number of layer 2–4 neurons is defective progenitor proliferation. To address this, we first assessed whether CIC is expressed in the progenitor cells in the embryonic cortex and found that to be the case (Supplementary Fig. 11a). Since layer 2–4 neurons are generated primarily around E14.5-E16.5 in mice[22], we assessed the proliferation of the cortical progenitors at E14.5 and E16.5 with a two-hour pulse-labeling of thymidine analog EdU (Ethynyl-2′-deoxyuridine). By combining EdU labeling with specific markers (TBR2 for intermediate progenitors and PAX6 for radial glia), we found that the numbers of progenitors and their proliferation rates (estimated from cells that were double-positive for EdU) remained unchanged in the mutant cortex (Supplementary Fig. 11b).

We next hypothesized that the reduction in the number of $CUX1^+$ cells is due to postnatal defects in neuronal maturation or maintenance. Indeed, the numbers of $CUX1^+$ and $SATB2^+$ neurons in layer 2–4 in the mutant cortex were similar to those of the controls at P0, but the numbers declined postnatally, and by P10 the numbers were comparable to those of 5-week old animals (Fig. 3a). Furthermore, we generated *Cic* conditional knockout mice using *Neurod6-Cre* (*NEX-Cre*), which has a spatial-temporal expression pattern similar to *Emx1-Cre* but is selective for post-mitotic excitatory neurons[23]. When we examined the cortex in post-mitotic conditional mutant mice, we still observed a reduction in the number of cells expressing CUX1 and SATB2 in layer 2–4 (Fig. 3b). These experiments suggest that the reduction in CUX1- and SATB2-expressing cells was caused by defects in post-mitotic neurons in the mutant cortex.

Increased apoptosis of upper layer neurons offers a potential explanation for the postnatal decline of $SATB2^+$ cells in layer 2–4 of mutant mice. To address this, we monitored cell death in P5 and P10 mutant cortex using activated caspase-3 (CASP3) immunostaining. We found more $CASP3^+$ cells in the upper layers of *Emx1-Cre* mutant cortex at P5, while the numbers of $CASP3^+$ cells were similar between mutant and control cortex at P10 (Supplemental Fig. 12). These results suggest a transient upregulation of apoptosis in the upper layers of P5 mutant cortex, consistent with the observed initial decline of $SATB2^+$ cells in layer 2–4 of mutant mice at P5.

CIC is critical for neuronal dendritic branching

Because CUX1 has roles in promoting dendritic branching[24,25] and CUX1 levels were reduced in the mutant cortex, we set out to examine the dendritic morphology of layer 2/3 neurons. To this end, we sparsely labeled P0 neurons using low-titer AAV virus with YFP [26]. We harvested brains when the animals were five weeks old and examined dendritic branching patterns of pyramidal neurons. Using Sholl analysis, we discovered that the mutant layer 2/3 pyramidal neurons displayed significantly reduced dendritic branching complexity compared to controls (Fig. 4a). The dendritic branching complexity of layer 5 pyramidal neurons did not differ from that of controls (Fig. 4b).

Deleting *Cic* in the hypothalamus and medial amygdala causes abnormal social interaction in mice

We next explored the neurobehavioral consequences of deleting the ATXN1-CIC complex outside of the *Emx1*-expressing domain. We utilized a Cre line that targets hypothalamic and medial amygdala neurons using the promoter from orthopedia homeobox (*Otp*)[27,28]. Using the *ROSA26*^{fsTRAP} reporter line to label Cre-positive cells[29]. We found that Cre was expressed in the medial amygdala (MeA) and multiple hypothalamic regions, including the paraventricular nucleus (PVN), supraoptic nucleus (SON), lateral hypothalamic area (LHA), as well as dorsomedial and ventromedial hypothalamic nuclei (DMH and VMH) (Supplementary Fig. 13). The expression pattern of *Otp-Cre* was consistent with the endogenous expression pattern of *Otp*, covering neuroendocrine neurons (e.g., PVN and SON) as well as regions that underlie social and emotional responses (VMH and MeA)[27,30–32]. We then generated *Otp-Cre Cic* conditional knockout mice and validated the knockout efficiency of *Cic* by confirming that the protein levels of CIC were greatly reduced in Cre-positive cells (Supplementary Fig. 14a).

To investigate whether CIC functions in *Otp*-lineage neurons to modulate neurobehavior, we performed a battery of behavioral tests. Interestingly, the *Otp-Cre* conditional mutant mice showed distinct behavioral defects in comparison to *Emx1-Cre* conditional mutants. The *Otp-Cre* conditional knockouts did not have abnormal behavior in the open-field, elevated plus-maze, or fear-conditioning assays (Fig. 5a and Supplementary Fig. 15), but they did show prominent social interaction deficits. In the three-chamber test, the conditional knockout mice interacted less with other mice (Fig. 5b). In the partition test, the conditional knockout mice spent less time interacting with novel mice, while the *Otp-Cre; Cic*$^{flox/+}$ mice showed an intermediate phenotype (Fig. 5c). In the resident-intruder test, the conditional knockout mice behaved more aggressively towards intruders, with more and longer attack episodes than controls (Fig. 5d). These results suggest that CIC has important functions in the medial amygdala and hypothalamus to modulate social interaction.

In contrast to the pronounced cortical layering defects in the *Emx1-Cre* knockout animals, we did not observe any gross histological abnormalities or altered cellularity of the *Otp*-lineage neurons in the *Otp-Cre* conditional mutants (Supplementary Fig. 14b and 16). Expression levels and patterns of several hypothalamic nuclei markers were also unaltered in mutant mice (Supplementary Fig. 17). Since CIC is a transcriptional regulator, we next examined gene expression profiles in *Otp*-lineage neurons to investigate the molecular changes leading to the social interaction deficits in the *Otp-Cre* mutant mice. To isolate RNAs specifically from these neurons, we applied the translating ribosome affinity purification (TRAP) approach using the Cre-dependent *ROSA*^{fsTRAP} mouse line[29], where the ribosomes are tagged with GFP in Cre-expressing cells. TRAP and RNA isolation was performed when animals were 8–10 weeks old[33]. RNAseq and gene expression analysis showed that a total of 207 genes were differentially expressed between *Otp-Cre; Cic*$^{flox/flox}$*; ROSA*^{fsTRAP} and *Otp-Cre;ROSA*^{fsTRAP} neurons, with 123 upregulated genes and 84 downregulated genes (FDR<0.05; Supplementary Fig. 18 and Supplementary Table 1). Known CIC targets *Etv4* and *Etv5* were among the most upregulated genes. Gene set analysis revealed that differentially expressed genes is significantly enriched for abnormal

nervous system morphology, abnormal synaptic transmission, and abnormal social/conspecific interaction (Fig. 5e). Notably, ten genes associated with abnormal synaptic transmission and eight genes associated with abnormal social/conspecific behavior showed more than 1.5-fold changes (Supplementary Table 2). We further validated a subset of genes from each group using quantitative real-time PCR (Supplementary Fig. 19). Dysregulation in the expression of these genes might contribute to the social behavioral deficits observed in the *Otp-Cre* mutant mice.

Heterozygous *CIC* truncating mutations cause a neurodevelopmental syndrome in human patients

Prior to our study, it was unclear whether loss-of-function mutations in *ATXN1* and *CIC* cause neurodevelopmental disorders, as no isolated truncating alleles had been identified for either gene. Our studies showed that the ATXN1-CIC complex plays critical roles in brain development that affect behavior, and that ATXN1 and ATXN1L execute their functions mainly through forming a complex with CIC. Guided by this knowledge and our prediction that homozygous loss-of-function in *CIC* would lead to premature lethality, we sought to identify patients with heterozygous loss-of-function mutations in *CIC*. It is also worth noting that *CIC* is predicted to be loss-of-function intolerant in the ExAC database (pLI = 1.00, Version 0.3.1)[34]. Although a 19:42796882 G/GC loss-of-function variant was reported in multiple individuals in the ExAC database, we found that the high frequency of this variant probably arises from sequencing/reporting errors or very low-grade mosaicism in the individuals. Thus the occurrence of this variant does not contradict the loss-of-function intolerance prediction from ExAC and our genetic findings below.

Through collaborative efforts, we identified four individuals from three families with heterozygous *de novo* truncating mutations in *CIC*, and one individual with an inherited nonsense variant from a father who is low-grade mosaic (see below) for the variant (Fig. 6a, b). Individuals 1 and 2-2 were part of exome trios. We additionally performed whole exome sequencing on individual 2-1. Individuals 3 and 4 were sequenced by whole exome sequencing with *de novo* variants confirmed through targeted Sanger sequencing of the parents. The *CIC* variants in all affected individuals were confirmed by Sanger sequencing. Besides the *CIC* variants, no variants were identified in known disease-causing genes that accounted for the clinical phenotypes. The five individuals had presented clinically with a spectrum of phenotypes, including developmental delay/intellectual disability (DD/ID), attention-deficit/hyperactivity disorder (ADHD), autism spectrum disorder (ASD), and seizures (Table 1, Supplementary Note).

Family 2 was notable for having two apparently affected siblings, and subsequent interrogation of the mutant allele in all six family members by Sanger sequencing found that the genotype segregated faithfully with the phenotype, suggesting germline mosaicism for the mutant allele in one of the parents (Supplementary Fig. 20). The father in family 4 is mosaic for the mutant allele (~15% mosaicism). By investigating the mutant allele in all family members using Sanger sequencing, we found that only the proband is heterozygous for the mutant allele, while the two unaffected brothers have only the wildtype allele (Supplementary Fig. 21). We examined the fibroblasts from patient 1 and found that both the

protein and RNA levels of *CIC* were reduced to almost 50% (Fig. 6c, d, Supplementary Fig. 22), supporting the idea that the mutation in patient 1 leads to nonsense-mediated decay and causes loss-of-function.

Discussion

In this study, we examined the roles of ATXN1-CIC complex in the developing nervous system and discovered a cell-type- and region-specific role for this complex in neurobehavioral functions. First, within the cortex, ATXN1-CIC complex is more important for upper layer neurons. Although CIC is expressed in all cortical layers and the protein was effectively removed from all layers in the *Emx1-Cre* conditional knockouts, the reduction of cortical thickness and cellular morphological defects were evident in the upper cortical layers while lower layers appeared intact. One explanation is that the ATXN1-CIC complex might have distinct downstream target genes in different cortical layers; it's also possible that other transcription factors compensate for the loss of CIC in the lower cortical layers. There has been rapid advancement in single-cell transcriptomic technologies, and studying the transcriptomic changes in different cell types at specific time points may provide insight into the possible mechanisms for the selective phenotype we observed.

The upper layer defects observed in *Emx1-Cre* conditional mutants are most likely driven by defects in postnatal maturation or maintenance of these neurons, as reduction in $SATB2^+$ neurons was evident only after postnatal day 5 (P5). This is further supported by our analyses of the *Neurod6-Cre* conditional knockout mice, suggesting that the reduction was due to defects in the post-mitotic neurons but not in their fate specification. Indeed, at P5, we observed a transient increase in the number of layer 2–4 neurons undergoing apoptosis in the *Emx1-Cre* mutant cortex, which could contribute to the postnatal reduction of $SATB2^+$ cells in layer 2–4. In addition, $SATB2^+$ cells in layer 2–4 from mutant cortex also expressed less *Cux1* RNA and the protein. The underlying mechanism leading to CUX1 reduction remains elusive, but evidence suggest that CUX1 dosage is critical for dendritic morphology of cortical neurons. Layer 2–3 neurons from $Cux1^{-/-}$ mice showed fewer dendritic branches and spines[24], whereas overexpression of *Cux1* in cultured cortical neurons increased spine density[25]. Therefore, in our studies, reduced CUX1 levels in *Emx1-Cre* mutant cortex could contribute to the observed dendritic arborization defects of upper layer neurons. Very recently, homozygous mutations in a human accelerated region (HAR) that could increase the expression of human *CUX1* were identified in patients with ASD and ID[25]. Our findings resonate with previous studies and highlight the importance of CUX1 dosage in modulating cognitive and social behavior outcome.

In some ADHD patients, brain imaging studies have identified cortical abnormalities[16], and there is a reduction in cortical thickness and a marked delay in the maturation across different brain regions[35,36]. Our *Emx1-Cre* conditional mutant animals provide evidence for the potential consequences of disrupting upper cortical layers in causing hyperactivity and learning deficit phenotypes. This provides an exciting opportunity to understand the contribution of specific cortical circuit defects to the clinical phenotypes of patients with ADHD. Upper layer neurons project axons that contribute to the corpus callosum, but the formation and thickness of the corpus callosum was unaffected in *Emx1-Cre* mutant mice.

This suggests that the formation of long range projections by upper layer neurons is anatomically normal, but it remains possible that they are functionally compromised.

Although the *Emx1-Cre* conditional mutants recapitulated the hyperactivity and learning/memory deficits seen in patients with heterozygous loss of *CIC*, the *Otp-Cre* knockout mice displayed phenotypes resembling ASD. The ventromedial hypothalamic (VMH) nuclei and medial amygdala (MeA), both targeted by the *Otp-Cre*, are activated in both aggressive and affiliative behavior[31,32]. Mis-expression of genes that influence synaptic transmission and social interaction might interfere with the synaptic plasticity and disrupt social brain circuits at the cellular level. For example, *Shank3*, which encodes a dosage-sensitive synaptic scaffold protein whose dysfunction is involved in human neuropsychiatric disorders, is significantly reduced in *Otp-Cre* mutant neurons. In *Otp-Cre* mutant neurons, the combinatorial effects of *Shank3* and other dysregulated genes that have reached their dysfunction thresholds might compromise healthy neuronal activity under social stimuli. Although the *Emx1-Cre* and *Otp-Cre* conditional knockouts together reproduced many clinical features of patients with *CIC* loss-of-function mutations, we did not observe overt seizures in any of our mutant mice by visual examinations ($Cic^{+/-}$, *Emx1-Cre* mutants, or *Otp-Cre* mutants). We also did not find any abnormalities in the electroencephalograms (EEGs) during two 8-hour recordings from $Cic^{+/-}$ or *Emx1-Cre* mutants (data not shown). We have, however, observed seizures in *Cic-L* $^{-/-}$ mice on a highly mixed background (Huda Y Zoghbi, personal observation). It is possible that seizures in the patients arise from dysfunction of forebrain inhibitory neurons, a cell type not covered by *Emx1-Cre*. Future studies with additional Cre drivers can help pinpoint the responsible cell types for seizures and elucidate possible underlying mechanisms.

In conclusion, studying the roles of ATXN1-CIC complex in the mouse brain has led us to identify new mutations underlying neuropsychiatric disease in humans. Our findings highlight distinct brain regions underlying the clinical symptoms in the patients and provide tractable models to further dissect the circuitries contributing to ADHD, learning deficits, and social behavior abnormalities. Our strategy underscores the value of model organisms in uncovering new syndromes and their pathophysiology. It is the findings in the *Emx1-Cre* and *Otp-Cre* driven *Cic* deletion mice that led us to search for patients with *CIC* loss-of-function mutations and informed us of the breadth of *CIC* haploinsufficiency manifestations. Two-way research between mouse models and human patients continues to reveal the neuronal and molecular bases of complex neurobehavioral disorders.

Online Methods

Human subjects

Patients were identified either by direct contact from family (family 1) or connections through GeneMatcher (family 2–4)[37]. Individuals 1 and 2-2 were part of exome trios (proband plus two biological parents). Individual 2-1 was subsequently enrolled in whole-exome sequencing study and her results were compared with the parents and individual 2-2. Probands 3 and 4 were sequenced by whole exome sequencing with *de novo* variants confirmed through targeted Sanger sequencing of the parents. The *CIC* variants in all affected individuals were confirmed by Sanger sequencing. Buccal swab DNAs from patient

2-2's three siblings were sent from GeneDx to Dr. Zoghbi's lab for the testing of *CIC* variants using Sanger sequencing. Fibroblasts from patient 1 were generated by Dr. Finnell's laboratory. Family 1 and 2 were enrolled under a research protocol approved by the Institutional Review Board of Baylor College of Medicine. Family 3 was enrolled under a research protocol approved by the Institutional Review Board of Mayo Clinic. All individuals or their guardians consented to participation in publication.

Statistical tests

Statistical tests were performed with GraphPad Prism. The details of the statistical tests and results are reported in Supplementary Table 3. For behavioral tests, values in all groups were assumed to be normally distributed. Welch's correction was used for t-tests when variances between groups were significantly different by F-test. Geisser–Greenhouse correction was used for one-way ANOVA

DNA Sanger sequencing of the proband's siblings in family 2

Buccal swab DNA samples in NaOH were retrieved from GeneDx and PCRs were performed using these sample. After PCR, the products amplified from the two unaffected siblings' DNAs were purified and then sent for Sanger sequencing. The PCR products amplified from the affected sibling's DNA were added with A-tails using a Taq polymerase and ligated into pGEM-T easy vectors (Promega). The ligation mixture was transformed into *E. coli* DH5α and colonies were isolated followed by plasmid purification (Nucleospin, Macherey Nagel).

Mouse models

All procedures in mice were approved by the Institutional Animal Care and Use Committee of Baylor College of Medicine. *Atxn1* null[3], *Atxn1l*^{flox}[9], *Emx1-Cre*[18], *Neurod6-Cre*[23], and *ROSA*^{fsTRAP}[29] have been described previously. To generate the *Otp-Cre* allele, bacterial artificial chromosomes (BAC) containing *Otp* (RP24-337G4) was modified using recombineering to replace the *Otp* coding sequence with *Cre*[38]. The modified BAC DNA was isolated and digested with BsiWI to release the transgene for pronuclear injection. Pups derived from the microinjected embryos were screened for the presence of the transgene. Transgenic founders were then mated to WT FVB mice and the offspring were screened for germline transmission. Transgenic mice with germline transmission were then backcrossed to the C57BL/6 background for more than seven generations.

Generation of *Cic*^{flox} and *Cic*^{null} alleles were carried out as follow. ES cells with *Cic*$^{tm1a(KOMP)Wtsi}$ allele were obtained from EUCOMM and were injected into C57BL/6 blastocysts. The *Cic*^{flox} mice were then generated by breeding to *Actin-FLP* mice to remove the genetrap cassette, and the *Cic*^{null} allele was generated by crossing to *CMV-Cre* mice (Supplementary Fig. 23). All mice were maintained on a C57BL/6 background. Day of plug was denoted E0.5 for timed-pregnant experiment. Primers for genotyping are reported in Supplementary Table 4. Both males and females were used, and we did not observe any gender difference in the phenotypes.

Antibodies

The following primary antibodies were used for western blot: rabbit polyclonal anti-ATXN1[2], rabbit polyclonal anti-ATXN1L[8], mouse monoclonal anti-VCL (Sigma, V9131), mouse monoclonal anti-GAPDH (Advanced ImmunoChemical Inc., 2-RGM2), and guinea pig polyclonal anti-CIC[7]. The primary antibodies used in immunofluorescence studies were: Rabbit anti-CUX1 (Santa Cruz, sc-13024), Rat anti-CTIP2 (Abcam, ab18465), Mouse anti-SATB2 (Abcam, ab51502), Rabbit anti-CIC (Generated in house using antigen described in[7]), Rabbit anti-PAX6 (Covance, PRB-278P), Rabbit anti-TBR2 (Abcam, ab23345), Chicken anti-GFP (Abcam, ab13970), Rabbit anti-CASP3 (Cell Signaling Technology #9661).

Behavioral tests

The open-field test, elevated plus maze test[39], low-dose amphetamine treatment[40], and fear conditioning[41] were performed as previously described. The three-chamber test was performed as previously described[39], with the modification that ambient light was maintained at 700–800 lux and white noise was used. The partition test was performed as previously described[39], with the modification that test mice were individually housed in standard housing cages separated into two compartments by a clear perforated Plexiglas barrier for one day. The resident-intruder test was performed as previously described[39] with the modification that male mice were singly housed for four weeks before testing to establish dominance. Tests were video-recorded and the episodes and time of attacks were analyzed.

Novel object recognition test was performed with the following protocol. During habituation, the test mouse was placed in the habituation arena and allowed to explore for 30 min. Following habituation, the test mouse was then introduced into the test arena where two identical objects (Legos) were placed with equal distance to the walls of the arena. The test mouse was allowed to explore the arena for 5 min (trial 1). After the first trial, the test mouse was returned to the habituation arena and the test arena and objects were cleaned with ethanol. On trials 1 to 3, identical objects were placed in the arena for the test mouse to explore and familiarize. On trial 4, a novel object, which was a Lego with a different color and shape than the familiar objects, was introduced into the test arena to replace one of the familiar objects. The test mouse was then allowed to explore the arena for 5 min. On trial 5, the familiar object replaced the novel object and was re-introduced back into the test arena. The amount of time that the test mouse spent on investigating (sniffing, climbing, and touching) the objects was recorded using the AnyMaze video tracking system. The test mouse was allowed to rest for at least 10 min between each trial.

Sample size in behavioral studies was estimated based on our previous experience with these behavioral tests. All behavioral tests were performed with the investigators blinded to the genotypes or treatment. In the low-dose amphetamine treatments, mice were assigned to either vehicle or amphetamine treatments using a list randomizer.

Hippocampal slice preparation and electrophysiology

Mice were anaesthetized by isoflurane inhalation and decapitated. The brain was isolated and immersed in chilled (2–5°C) cutting solution containing (in mM) 220 sucrose, 2.5 KCl, 0.5 $CaCl_2$, 7 $MgCl_2$, 1.25 NaH_2PO_4, 25 $NaHCO_3$, 7 D-glucose. Transverse hippocampal slices (400 μm) were prepared with a vibratome (Leica Microsystems Inc., Buffalo Grove, IL). The slices were incubated at 37°C for 30 minutes in artificial cerebrospinal fluid (ACSF) containing (in mM) 125 NaCl, 2.5 KCl, 2 $CaCl_2$, 1 $MgCl_2$, 1.25 NaH_2PO_4, 25 $NaHCO_3$, and 14.83 D-glucose, and then transferred to room temperature for another 30 minutes before recording.

Extracellular stimuli were administered along the Schaffer collaterals using a bipolar tungsten stimulation electrode (WPI), field excitatory postsynaptic potentials (fEPSPs) were recorded in stratum radiatum. The recording pipettes were filled with 2 M NaCl (1–2 MΩ) and their distance to the stimulating electrode were kept constant (~300 μm). Input/output (I/O) curves were generated using incremental stimulus intensities and were used to assess baseline synaptic transmission. All subsequent stimuli were set to an intensity that evoked a 30–40% of the maximum fEPSP slope. Paired pulse facilitation was assessed via systematic stimuli with different interval (25, 50, 100, 200, and 400 mSec). The paired pulse ratio was obtained by dividing the rising slope of the second fEPSP with the rising slope of the first fEPSP. For LTP experiments, stable baseline fEPSPs were recorded for 20 min, and then LTP was induced by 2 trains of high-frequency stimulation (HFS, 100 Hz for 1 s) with 20 s intertrain interval. The magnitude of potentiation was determined by measuring the rising slope of the fEPSP.

The recordings were made using Multiclamp 700B amplifiers (Molecular Devices, Union City, CA). Data acquisition and analysis were performed using digitizer DigiData 1440A and analysis software pClamp 10 (Molecular Devices). Signals were filtered at 2 kHz and sampled at 10 kHz. All recordings were performed at 30 ± 1°C by using an automatic temperature controller (Warner Instrument, Hamden, CT).

Co-immunoprecipitation (Co-IP)

The cortex or hypothalamus were dissected from an 8-week old wildtype mouse and homogenized in 500 μL of extraction buffer (75 mM NaCl, 5 mM $MgCl_2$, 50 mM Tris pH 8.0, 0.5% Triton X-100, supplemented with fresh protease inhibitors and phosphatase inhibitors). The homogenates were then centrifuged at 13,200 rpm for 15 min at 4 °C. The supernatants were diluted five times using the extraction buffer without any detergent. For each IP, 20 μL of prepared Dynabeads Protein A (Novex, Life Technology) was added to 500 μL of the diluted extracts, together with 1 μL of rabbit anti-CIC antibody or normal rabbit IgG. IP reactions were performed overnight at 4 °C with gentle head-to-tail rotations. The beads were then washed three times with the extraction buffer (with detergent) and proteins bound to the beads were eluted with SDS sample loading buffer. Co-IP samples were analyzed using western blot.

Column fractionation and analysis

Gel-filtration (sizing) chromatography was performed as previously described[42] using cortex or hypothalamus from five 8-week old animals. For each column chromatography, 4 mg of total proteins were loaded to the column for analysis.

Histology

Samples were dissected and fixed in 4% paraformaldehyde in PBS or 10% neutral buffered formalin for 24–48 hours. The tissues were then incubated in 70% ethanol for 24 hours, 95% ethanol overnight, 100% ethanol for 4 hours, chloroform overnight, and paraffin for four hours twice. The tissues were then embedded in paraffin and sectioned at 8-μm thickness. Nissl (cresyl violet) staining and luxol fast blue staining were performed using standard protocols.

Immunofluorescence Staining and TUNEL assay

For *Emx1-Cre* and *Neurod6-Cre* mutant studies, the animals were anesthetized and transcardialy perfused with 4% paraformaldehyde in PBS. Tissues were collected and fixed in 4% paraformaldehyde in PBS at 4°C overnight. The tissues were cryoprotected in 15% and 30% sucrose in PBS, and then imbedded and frozen in Tissue-Tek® OCT compound. Tissues were sectioned at 25-μm thickness and mounted on *Superfrost Plus* Microscope Slides and air-dried, followed by rehydration in PBS. For *Otp-Cre* studies, brain tissues were directly frozen in Tissue-Tek® OCT compound and sectioned at 25-μm thickness and mounted on *Superfrost Plus* Microscope Slides. Prior to staining, the slides were fixed in 10% neutral buffered formalin for 15 mins, and washed three times with PBS. All slides were blocked in blocking buffer at room temperature for 1 hour, following by incubating with primary antibodies in blocking buffer at 4°C overnight. The slides were washed with 0.1% Triton X-100 in PBS three times, and incubated with secondary antibodies in blocking buffer at room temperature for two hours. The slides were then washed with 0.1% Triton X-100 in PBS two times, counterstained with DAPI, washed with 0.1% Triton X-100 in PBS once and PBS once. Slides were mounted with coverslips with ProLong Gold or ProLong Diamond (Molecular Probes). When needed, antigen retrieval was performed before blocking using Antigen Unmasking Solution (Vector Laboratory, Citric Acid Based) at 95°C for 20–60 minutes and cool for at least 20 minutes at room temperature. The slides were then washed in PBS three times and then blocked and stained as described above.

TUNEL assays were performed using the Click-iT® Plus TUNEL assay kit (with Alexa Fluor 488 Dye, Molecular Probes) with minor modifications: 25-μm thick, air-dried cryo-sections mounted on the slides were used for the assay; in addition to the proteinase K treatment recommended by the manufacturer, an additional 700 μg of proteinase K (at 1 mg/ml) was added to each slide and the slides were incubated for 70 min at room temperature; after the TUNEL assay, the sections were counter-stained with DAPI.

EdU (5-ethynyl-2′-deoxyuridine) labeling

50 mg/kg of EdU (Santa Cruz, sc-284628) was injected intraperitoneally into timed-pregnant female mice. Two hours later, injected mice were euthanized, and embryonic brains were dissected and fixed overnight. The tissues were then cryo-protected and sectioned as

described in the Immunofluorescent Staining section. EdU was labeled with Click-iT® EdU Alexa Fluor® Imaging Kit (Thermo) before immunofluorescent staining.

Image acquisition and analysis

Confocal images were acquired with Leica TCS SP8 or ZEISS LSM 880. Epifluorescence images were acquired with Leica DM4000 microscope. Light microscopy images were acquired with Leica DM4000 or Zeiss Axio Scan.Z1 slide scanner. For cell counting, images from parietal cortices were cropped at 200-μm bins and were quantified with Fiji using the Cell Counter plugin[43]. The thickness of pyramidal layers of CA1 and CA3, as well as the thickness of granule layer of DG were measured using Fiji. All analyses were performed with the experimenter blinded to the genotype.

Dendritic branching analysis

AAV-YFP (AAV8 with CBA-YFP-2A-YFP-2A-YFP) was generated and injected into lateral ventricles as previously described[26]. To achieve sparse labeling, 4.8×10^7 viral particles were injected into each ventricle. At 5 weeks of age, the animals were anesthetized and transcardialy perfused with 4% PFA in PBS. Brains were collected and fix in 4% PFA in PBS at 4°C overnight. 100 μm sections were obtained with Leica vibratome. The sections were mounted on *Superfrost Plus* Microscope Slides and coverslipped with VECTASHIELD (Vector Laboratories). Pyramidal neurons were identified based on their morphology and location. Z-stack images were taken with ZEISS LSM 880. Neuronal structure reconstruction and Scholl analysis was performed with Neurolucida 360 software (MBF Bioscience).

In situ hybridization

RNA *in situ* hybridization was performed on adult mouse brain sections. The DNA templates for the *in situ* hybridization probes were amplified from mouse brain cDNA and cloned into pGEMT-Easy vectors. To generate DIG-labeled mRNA probes *in vitro* transcription was performed using a kit from Roche according to the manufacturer's instruction. The primers and further information about the probes are listed in Supplementary Table 4. Adult mouse brains were collected and immediately embedded and frozen in Tissue-Tek® OCT compound. Coronal sections were collected from the somatosensory cortex at 25-μm thickness. *In situ* hybridization was performed as previously described[44] and the stained slides were imaged using a Zeiss Axio Scan.Z1 slide scanner.

Quantitative reverse transcription PCR

RNA was extracted with TRIzol and reverse transcribed using M-MLV Reverse Transcriptase (Thermo). Real-time PCR was performed with PerfeCTa SYBR Green FastMix ROX (Quanta Biosciences) or iTaq™ Universal SYBR® Green (BIO-RAD). Primers are listed in Supplementary Table 4. *Rps16* was used as the reference gene, and fold changes were calculated using the $2^{-\Delta\Delta Ct}$ method[45,46]. In short, the mean of the threshold cycle (Ct) of three technical replicates was used as the Ct of a given animal.

$$\Delta Ct_{(Animal)} = Ct_{(Target)} - Ct_{(S16)}$$
$$2^{-\Delta\Delta Ct} = 2^{-(Mean\ \Delta Ct_{(Mutant)} - Mean\ \Delta Ct_{(Control)})}$$

ANOVA or t test was performed on the ΔCt values[46]. The confidence intervals of ΔΔCt values were calculated, and the confidence intervals of $2^{-\Delta\Delta Ct}$ values were plotted in the figures and reported in Supplementary Table 3[46].

Translating ribosome affinity purification (TRAP) and RNA profiling

TRAP profiling was performed as previously described[29,33]. Briefly, hypothalamus and adjacent amygdala regions were dissected from 8–10 weeks-old male mice. Tissues were homogenized in 3 mL of homogenization buffer and 60 μg each of 19C8 and 19F7 was used for every immunoprecipitation experiment. The subsequent sample quality check and processing of the purified RNA was performed by the Genomic and RNA Profiling Core at Baylor College of Medicine. Using NuGEN Ovation RNA-Seq System v2, purified double-stranded cDNA was generated. For validation, real-time PCR was performed with iTaq™ Universal SYBR® Green (BIO-RAD). Primers are listed in Supplementary Table 4. *Rps16*, *Hprt*, and *Gapdh* were used as reference genes, and fold changes were calculated using the $2^{-\Delta\Delta Ct}$ method[45,46].

RNAseq data analysis

For each sample, about 100 million pairs of 100 bp pair-end reads were generated. Raw reads were trimmed before mapping to reference genome. Trimmed reads were then aligned to the *Mus musculus* genome (UCSC mm10) using TopHat v2.0.9[47] with default parameters. The mappability for all 8 samples was about 50%. HTSeq[48] was used to obtain read counts. Using the obtained read counts, differential gene analysis was carried out using the DESeq package in the R environment. A gene was identified as significantly changed if falls under the FDR of 5%.

Phenotype association analyses were performed using the WebGestalt (WEB-based GEne SeT AnaLysis) Toolkit[49,50].

Supplementary Material

Refer to Web version on PubMed Central for supplementary material.

Acknowledgments

We thank the families for their participation in the study and Dr. Hui Zheng for providing *Neurod6-Cre* (*NEX-Cre*) mice. The project was support by grants NIH/NICHD R01 HD081216 and HD083809 to R.H.F.; NIH/NHGRI 1UM1HG008898-01 to M.N.B.; NIH/NINDS R37 NS22920 to H.T.O.; NIH/NINDS R01 NS089664 to R.V.S., NIH/NINDS R01 NS027699-26 and R37 NS027699-28 to H.Y.Z. Q.T. was supported by NIH/NINDS F32 NS083091 and M.W.C.R. received support from Canadian Institutes of Health Research Fellowship 201210MFE-290072–173743. H.Y.Z. is an investigator of the Howard Hughes Medical Institute. We thank the RNA In Situ Hybridization Core (supported by a Shared Instrumentation grant 1S10OD016167), and the Microscopy Core, and the Neuropathology Core at Baylor College of Medicine. All three cores are supported by the NIH IDDRC grant U54HD083092 from the Eunice Kennedy Shriver National Institute of Child Health & Human Development. The content is solely the responsibility of the authors and does not necessarily represent the official views of the Eunice Kennedy Shriver National Institute of Child Health & Human Development or the National

Institutes of Health. This project was partly supported by the Genomic and RNA Profiling Core at Baylor College of Medicine and the expert assistance of the core director, Dr. Lisa D. White, Ph.D. We would like to thank the Mayo Clinic Center for Individualized Medicine Investigative and Functional Genomics Program for funding and support.

References

1. Orr HT, et al. Expansion of an unstable trinucleotide CAG repeat in spinocerebellar ataxia type 1. Nat Genet. 1993; 4:221–6. [PubMed: 8358429]
2. Burright EN, et al. SCA1 transgenic mice: a model for neurodegeneration caused by an expanded CAG trinucleotide repeat. Cell. 1995; 82:937–48. [PubMed: 7553854]
3. Matilla A, et al. Mice lacking ataxin-1 display learning deficits and decreased hippocampal paired-pulse facilitation. J Neurosci. 1998; 18:5508–16. [PubMed: 9651231]
4. Watase K, et al. A long CAG repeat in the mouse Sca1 locus replicates SCA1 features and reveals the impact of protein solubility on selective neurodegeneration. Neuron. 2002; 34:905–19. [PubMed: 12086639]
5. Asher M, Johnson A, Zecevic B, Pease D, Cvetanovic M. Ataxin-1 regulates proliferation of hippocampal neural precursors. Neuroscience. 2016
6. Lin X, Antalffy B, Kang D, Orr HT, Zoghbi HY. Polyglutamine expansion down-regulates specific neuronal genes before pathologic changes in SCA1. Nat Neurosci. 2000; 3:157–63. [PubMed: 10649571]
7. Lam YC, et al. ATAXIN-1 interacts with the repressor Capicua in its native complex to cause SCA1 neuropathology. Cell. 2006; 127:1335–47. [PubMed: 17190598]
8. Bowman AB, et al. Duplication of Atxn1l suppresses SCA1 neuropathology by decreasing incorporation of polyglutamine-expanded ataxin-1 into native complexes. Nat Genet. 2007; 39:373–9. [PubMed: 17322884]
9. Lee Y, et al. ATXN1 protein family and CIC regulate extracellular matrix remodeling and lung alveolarization. Dev Cell. 2011; 21:746–57. [PubMed: 22014525]
10. Fryer JD, et al. Exercise and genetic rescue of SCA1 via the transcriptional repressor Capicua. Science. 2011; 334:690–3. [PubMed: 22053053]
11. Celestino-Soper PB, et al. Deletions in chromosome 6p22.3-p24.3, including ATXN1, are associated with developmental delay and autism spectrum disorders. Mol Cytogenet. 2012; 5:17. [PubMed: 22480366]
12. Baroy T, et al. Haploinsufficiency of two histone modifier genes on 6p22.3, ATXN1 and JARID2, is associated with intellectual disability. Orphanet J Rare Dis. 2013; 8:3. [PubMed: 23294540]
13. Di Benedetto D, et al. 6p22.3 deletion: report of a patient with autism, severe intellectual disability and electroencephalographic anomalies. Mol Cytogenet. 2013; 6:4. [PubMed: 23324214]
14. Vissers LE, et al. A de novo paradigm for mental retardation. Nat Genet. 2010; 42:1109–12. [PubMed: 21076407]
15. Athanasakis E, et al. Next generation sequencing in nonsyndromic intellectual disability: from a negative molecular karyotype to a possible causative mutation detection. Am J Med Genet A. 2014; 164A:170–6. [PubMed: 24307393]
16. Giedd JN, Rapoport JL. Structural MRI of pediatric brain development: what have we learned and where are we going? Neuron. 2010; 67:728–34. [PubMed: 20826305]
17. Ecker C, Bookheimer SY, Murphy DG. Neuroimaging in autism spectrum disorder: brain structure and function across the lifespan. Lancet Neurol. 2015; 14:1121–34. [PubMed: 25891007]
18. Gorski JA, et al. Cortical excitatory neurons and glia, but not GABAergic neurons, are produced in the Emx1-expressing lineage. J Neurosci. 2002; 22:6309–14. [PubMed: 12151506]
19. Sotnikoca, TD., Gainedinov, RR. Attention-decifit hyperactivity disorder. In: Pietropaolo, S.Sluyter, F., Crusio, WE., editors. Behavioral Genetics of the Mouse: Volume 2, Genetic Mouse Models of Neurobehavioral Disorders. Vol. 2. Cambridge University Press; 2014. p. 164-72.
20. Jonas P, Lisman J. Structure, function, and plasticity of hippocampal dentate gyrus microcircuits. Frontiers in Neural Circuits. 2014; 8

21. Fame RM, MacDonald JL, Macklis JD. Development, specification, and diversity of callosal projection neurons. Trends Neurosci. 2011; 34:41–50. [PubMed: 21129791]
22. Hevner RF, et al. Beyond laminar fate: toward a molecular classification of cortical projection/pyramidal neurons. Dev Neurosci. 2003; 25:139–51. [PubMed: 12966212]
23. Goebbels S, et al. Genetic targeting of principal neurons in neocortex and hippocampus of NEX-Cre mice. Genesis. 2006; 44:611–21. [PubMed: 17146780]
24. Cubelos B, et al. Cux1 and Cux2 regulate dendritic branching, spine morphology, and synapses of the upper layer neurons of the cortex. Neuron. 2010; 66:523–35. [PubMed: 20510857]
25. Doan RN, et al. Mutations in Human Accelerated Regions Disrupt Cognition and Social Behavior. Cell. 2016; 167:341–354. e12. [PubMed: 27667684]
26. Kim JY, et al. Viral transduction of the neonatal brain delivers controllable genetic mosaicism for visualising and manipulating neuronal circuits in vivo. Eur J Neurosci. 2013; 37:1203–20. [PubMed: 23347239]
27. Acampora D, et al. Progressive impairment of developing neuroendocrine cell lineages in the hypothalamus of mice lacking the Orthopedia gene. Genes Dev. 1999; 13:2787–800. [PubMed: 10557207]
28. Diaz C, Morales-Delgado N, Puelles L. Ontogenesis of peptidergic neurons within the genoarchitectonic map of the mouse hypothalamus. Front Neuroanat. 2014; 8:162. [PubMed: 25628541]
29. Zhou P, et al. Interrogating translational efficiency and lineage-specific transcriptomes using ribosome affinity purification. Proc Natl Acad Sci U S A. 2013; 110:15395–400. [PubMed: 24003143]
30. Alvarez-Bolado G, Grinevich V, Puelles L. Editorial: Development of the hypothalamus. Front Neuroanat. 2015; 9:83. [PubMed: 26157363]
31. Kim Y, et al. Mapping social behavior-induced brain activation at cellular resolution in the mouse. Cell Rep. 2015; 10:292–305. [PubMed: 25558063]
32. Kas MJ, Modi ME, Saxe MD, Smith DG. Advancing the discovery of medications for autism spectrum disorder using new technologies to reveal social brain circuitry in rodents. Psychopharmacology (Berl). 2014; 231:1147–65. [PubMed: 24522332]
33. Mellen M, Ayata P, Dewell S, Kriaucionis S, Heintz N. MeCP2 binds to 5hmC enriched within active genes and accessible chromatin in the nervous system. Cell. 2012; 151:1417–30. [PubMed: 23260135]
34. Lek M, et al. Analysis of protein-coding genetic variation in 60,706 humans. Nature. 2016; 536:285–291. [PubMed: 27535533]
35. Shaw P, et al. Attention-deficit/hyperactivity disorder is characterized by a delay in cortical maturation. Proc Natl Acad Sci U S A. 2007; 104:19649–54. [PubMed: 18024590]
36. Shaw P, et al. Longitudinal mapping of cortical thickness and clinical outcome in children and adolescents with attention-deficit/hyperactivity disorder. Arch Gen Psychiatry. 2006; 63:540–9. [PubMed: 16651511]
37. Sobreira N, Schiettecatte F, Valle D, Hamosh A. GeneMatcher: a matching tool for connecting investigators with an interest in the same gene. Hum Mutat. 2015; 36:928–30. [PubMed: 26220891]
38. Warming S, Costantino N, Court DL, Jenkins NA, Copeland NG. Simple and highly efficient BAC recombineering using galK selection. Nucleic Acids Res. 2005; 33:e36. [PubMed: 15731329]
39. Chao HT, et al. Dysfunction in GABA signalling mediates autism-like stereotypies and Rett syndrome phenotypes. Nature. 2010; 468:263–9. [PubMed: 21068835]
40. Han K, et al. SHANK3 overexpression causes manic-like behaviour with unique pharmacogenetic properties. Nature. 2013; 503:72–7. [PubMed: 24153177]
41. Crespo-Barreto J, Fryer JD, Shaw CA, Orr HT, Zoghbi HY. Partial loss of ataxin-1 function contributes to transcriptional dysregulation in spinocerebellar ataxia type 1 pathogenesis. PLoS Genet. 2010; 6:e1001021. [PubMed: 20628574]
42. Park J, et al. RAS-MAPK-MSK1 pathway modulates ataxin 1 protein levels and toxicity in SCA1. Nature. 2013; 498:325–331. [PubMed: 23719381]

43. Schindelin J, et al. Fiji: an open-source platform for biological-image analysis. Nat Methods. 2012; 9:676–82. [PubMed: 22743772]
44. Yaylaoglu MB, et al. Comprehensive expression atlas of fibroblast growth factors and their receptors generated by a novel robotic in situ hybridization platform. Dev Dyn. 2005; 234:371–86. [PubMed: 16123981]
45. Schmittgen TD, Livak KJ. Analyzing real-time PCR data by the comparative C(T) method. Nat Protoc. 2008; 3:1101–8. [PubMed: 18546601]
46. Yuan JS, Reed A, Chen F, Stewart CN Jr. Statistical analysis of real-time PCR data. BMC Bioinformatics. 2006; 7:85. [PubMed: 16504059]
47. Kim D, et al. TopHat2: accurate alignment of transcriptomes in the presence of insertions, deletions and gene fusions. Genome Biol. 2013; 14:R36. [PubMed: 23618408]
48. Anders S, Pyl PT, Huber W. HTSeq--a Python framework to work with high-throughput sequencing data. Bioinformatics. 2015; 31:166–9. [PubMed: 25260700]
49. Wang J, Duncan D, Shi Z, Zhang B. WEB-based GEne SeT AnaLysis Toolkit (WebGestalt): update 2013. Nucleic Acids Res. 2013; 41:W77–83. [PubMed: 23703215]
50. Zhang B, Kirov S, Snoddy J. WebGestalt: an integrated system for exploring gene sets in various biological contexts. Nucleic Acids Res. 2005; 33:W741–8. [PubMed: 15980575]

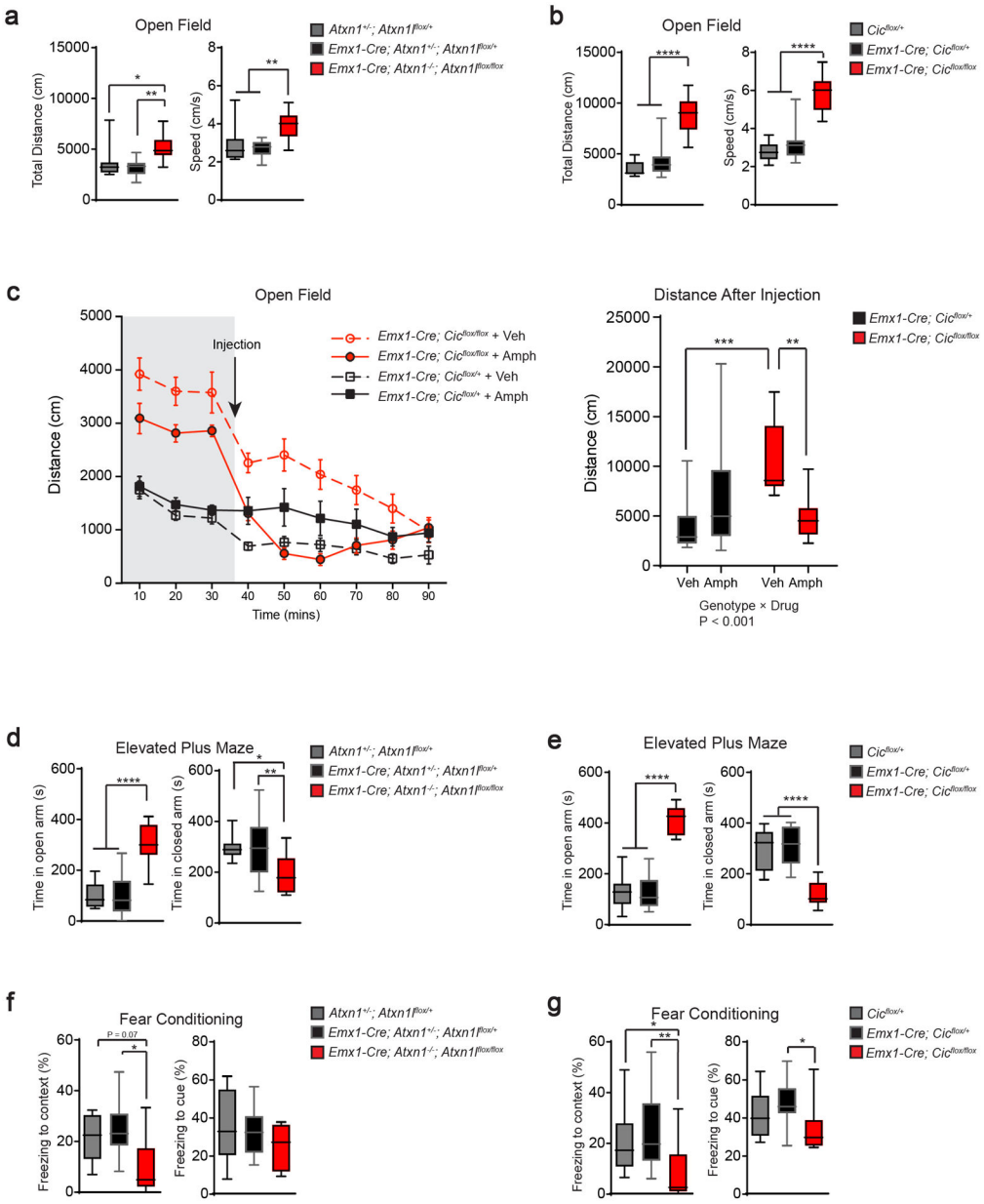

Figure 1. Deleting *Atxn1-Atxn1l* or *Cic* in the developing forebrain results in behavioral abnormalities

(**a, b**) In the open field test, both *Atxn1-Atxn1l* and *Cic* conditional knockout mice showed increased exploratory activities as demonstrated by increased total distance travelled and increased movement speed (n = 9–16, 12–13 weeks old). (**c**) After recording 30 minutes of baseline activity, we administered low-dose amphetamine (2 mg/kg body weight) and monitored locomotion for 60 minutes. Low-dose amphetamine calmed the *Cic* conditional knockout mice (n = 10–14, 12–13 weeks old). (**d, e**) In the elevated plus maze test, both mutant mice spent more time in the open arm and less time in the closed arm (n = 11–18, 12–13 weeks old). (**f, g**) Both mutant mouse lines had reduced freezing in the fear conditioning test (n = 8–13, 16–20 weeks old). Data are represented as mean ± s.e.m. in the

left panel of **1c**. All Other data are presented in box-and-whisker plots, with center lines represent median, box limits represent interquartile range, and whiskers represent minimum to maximum data range. *: $P < 0.05$; **: $P < 0.01$; ***: $P < 0.001$; ****: $P < 0.0001$

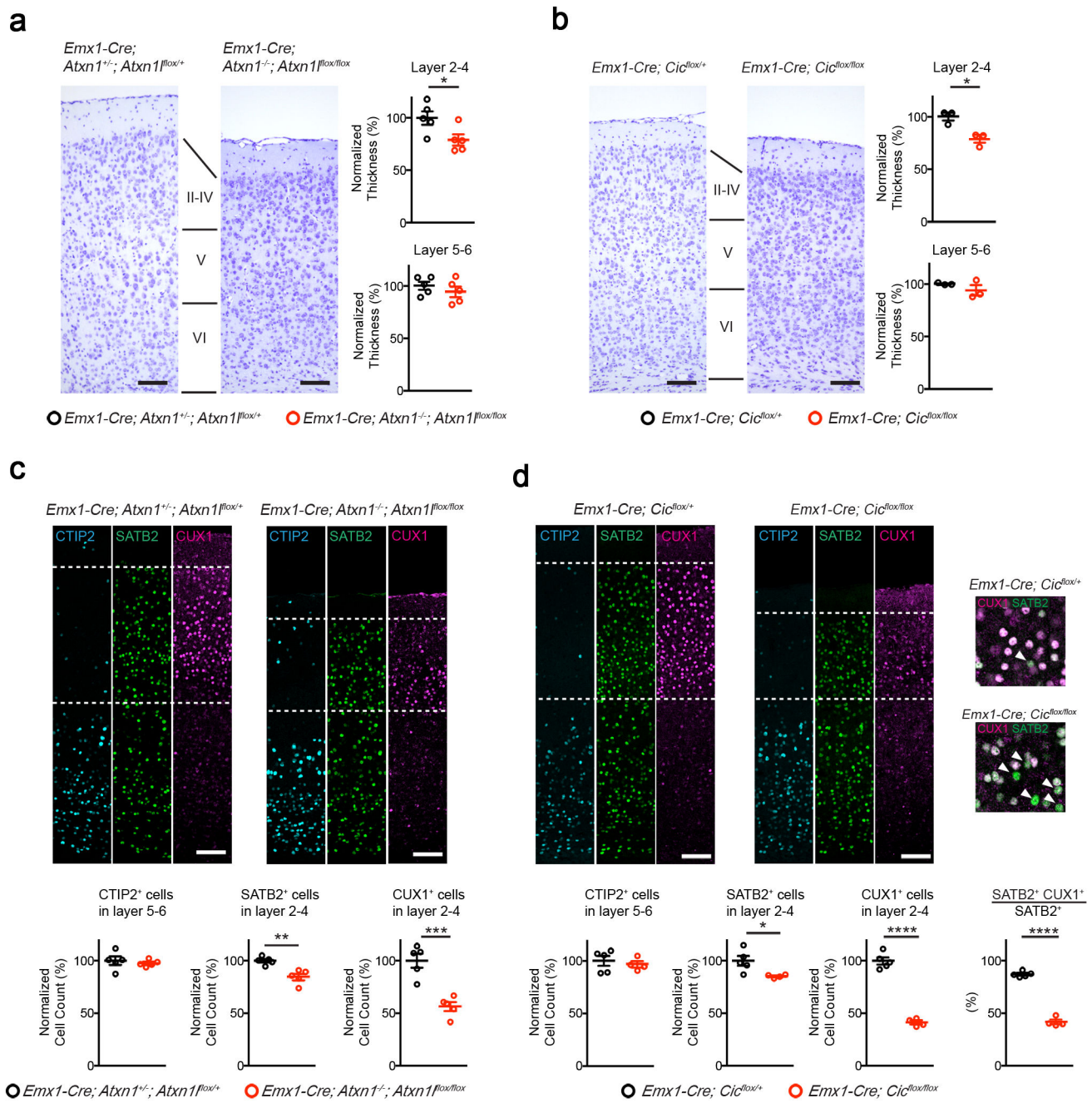

Figure 2. Deleting *Atxn1-Atxn1l* or *Cic* in the developing forebrain results in reduced thickness of upper cortical layers

(**a, b**) By Nissl staining, both mutant mouse lines had reduced thickness of layer 2–4, but not layer 5–6 (n = 3–5, scale bar = 100 μm). (**c, d**) Immunofluorescent staining of the cortex from 5-week old control and mutant animals. The number of CTIP2$^+$ cells in layer 5–6 did not change, but the numbers of SATB2$^+$ and CUX1$^+$ cells were reduced in the mutant cortex (n = 4–5, scale bar = 100 μm). (**d**, inset) Mutant mice showed fewer layer 2–4 SATB2$^+$ cells coexpressing CUX1. (Arrowhead: SATB2 single positive cells.) Data are represented as mean ± s.e.m. *: $P < 0.05$; **: $P < 0.01$; ***: $P < 0.001$; ****: $P < 0.0001$

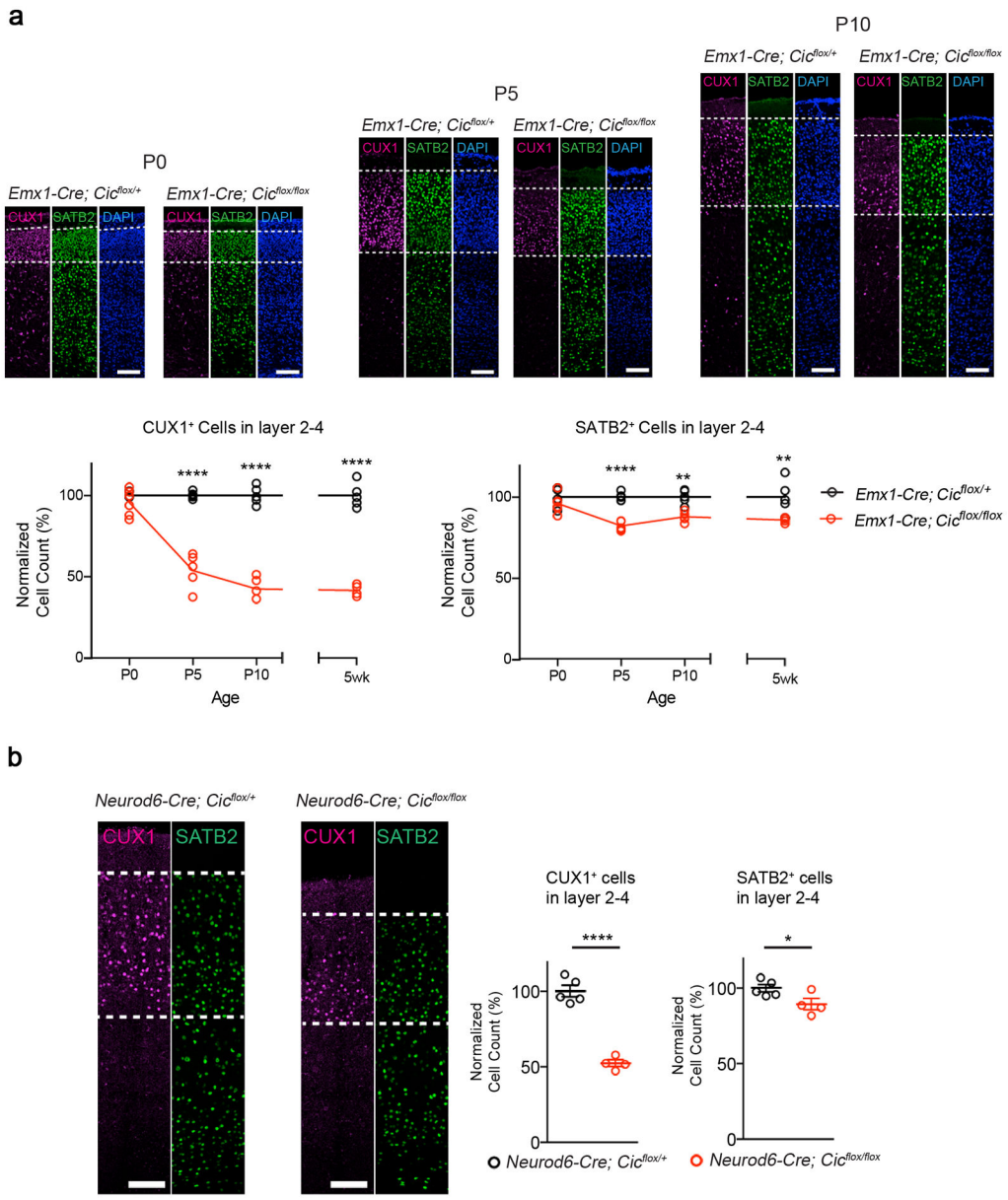

Figure 3. The histological defects in *Emx1-Cre Cic* mutant animals occur postnatally in post-mitotic neurons

(**a**) The numbers of CUX1$^+$ cells and SATB2$^+$ cell in layer 2–4 diminished postnatally. Immunofluorescent staining with CUX1 and SATB2 revealed that the number of CUX1$^+$ cells and SATB2$^+$ cells at P0 were comparable among control and mutant animals. The number gradually decreased in the mutant mice, and by P10 the numbers were comparable to those from 5-week old animals (n = 4–6, scale bar = 100 μm). (The 5-week old data are from Figure 2.) (**b**) Immunofluorescent staining with CUX1 and SATB2 revealed that the numbers of layer 2–4 CUX1$^+$ and SATB2$^+$ cells were reduced in *Neurod6-Cre* conditional mutants, which removes *Cic* in post-mitotic neurons (n = 4–5, scale bar = 100 μm). Data are represented as mean ± s.e.m. *: $P < 0.05$; ****: $P < 0.0001$

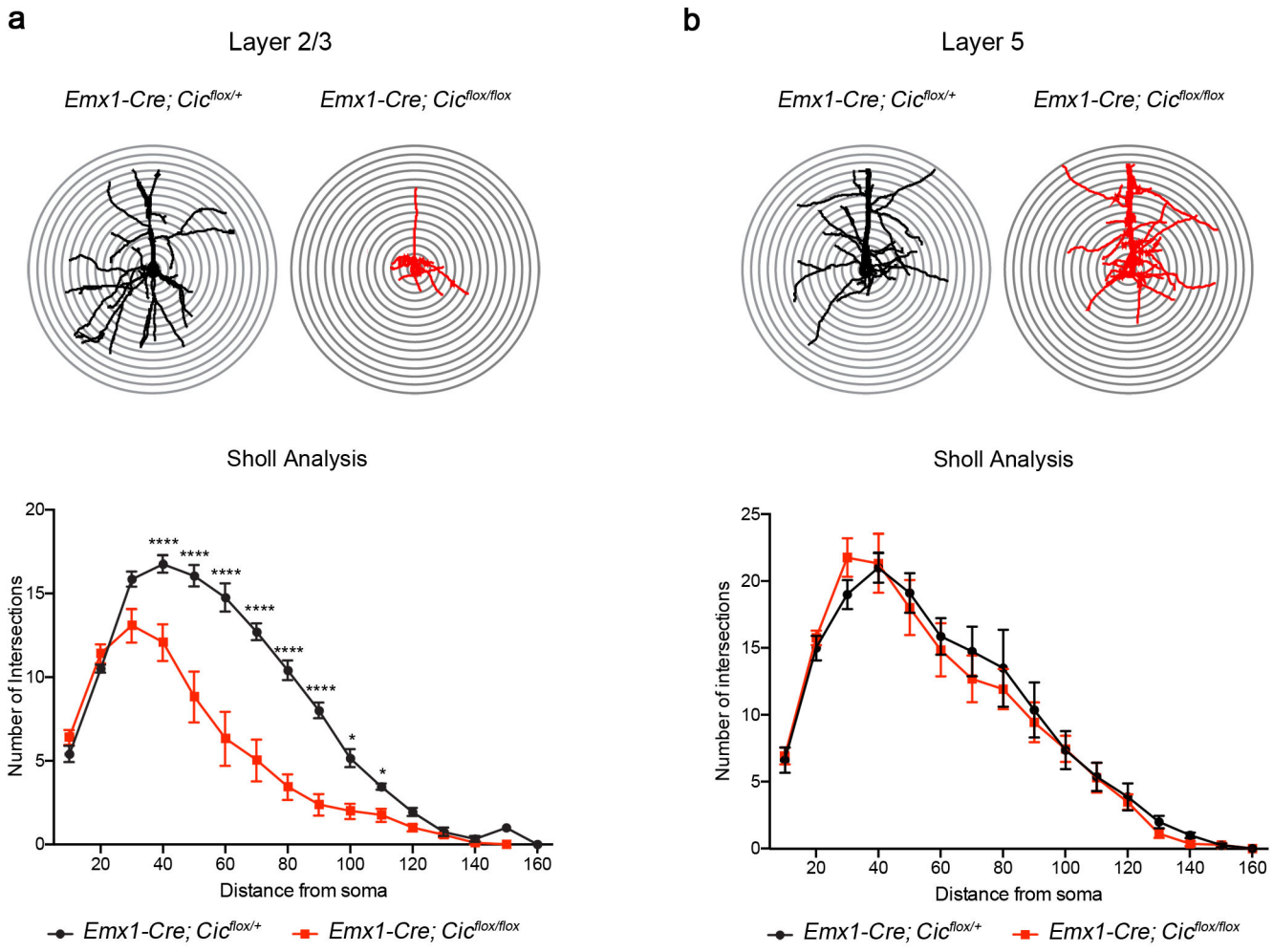

Figure 4. Morphological defects in layer 2/3 pyramidal neurons in the *Emx1-Cre Cic* conditional knockout mice

(a) Sholl analysis showed that mutant layer 2/3 pyramidal neurons had reduced dendritic complexity as compared with control animals. **(b)** The dendritic complexity in layer 5 neurons was not affected in mutant mice (n = 4–6 animals, 2–4 cells per animal). Data are represented as mean ± s.e.m. *: $P < 0.05$; ****: $P < 0.0001$

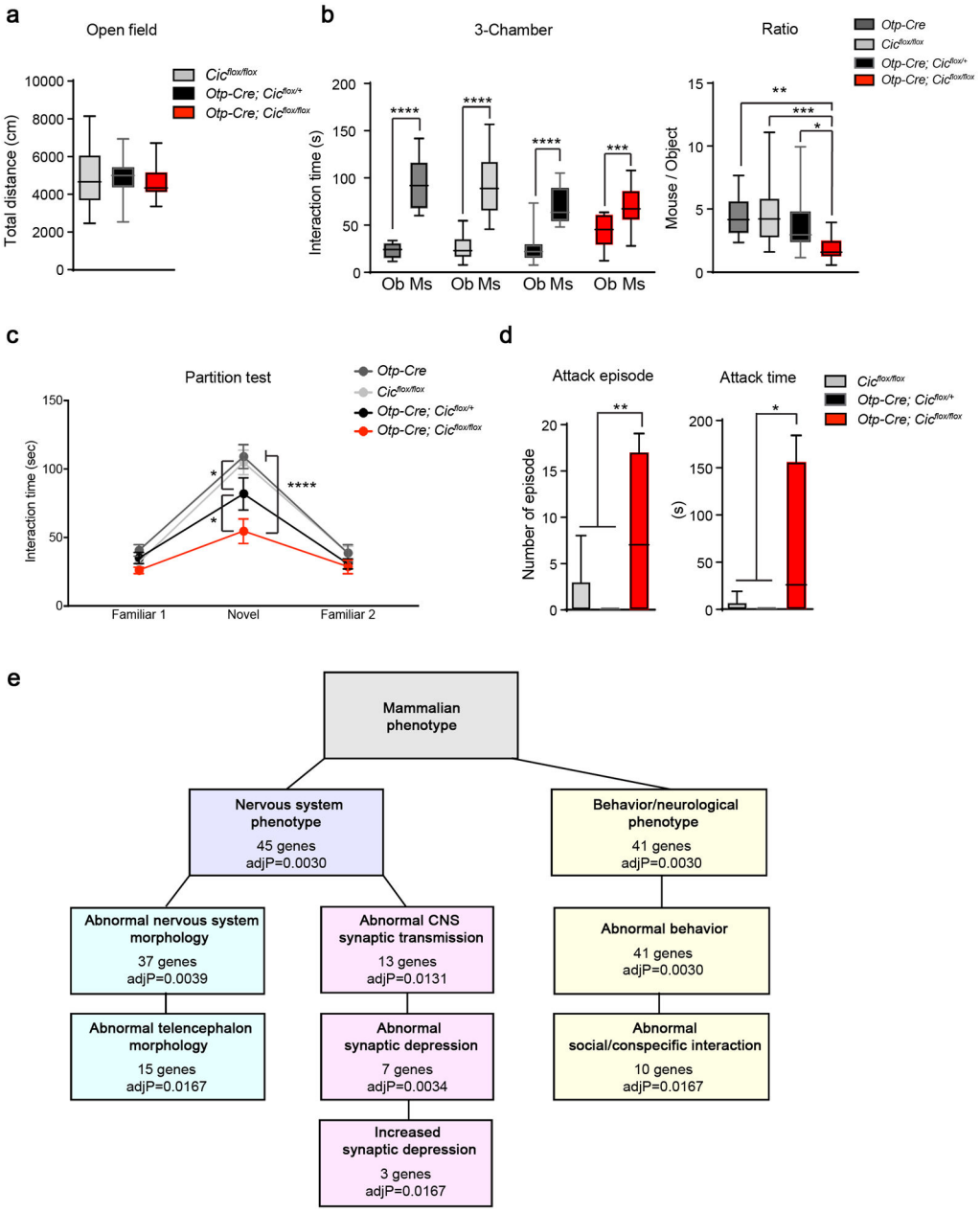

Figure 5. Deleting *Cic* from the hypothalamus and medial amygdala results in abnormal social behavior

(**a**) The *Otp-Cre* conditional knockout mice showed normal exploratory activities in the open-field test (n = 16–28, 8–12 weeks old). (**b**) In the three-chamber test, the *Otp-Cre* conditional mutant animals still preferred mouse (Ms) over object (Ob), but they spent less time with mouse as compare to controls (n = 15–19, 8–12 weeks old). (**c**) In the partition test, the *Otp-Cre; Cic*$^{flox/flox}$ mice spent less time interacting with the novel partner mice. The *Otp-Cre; Cic*$^{flox/+}$ mice had an intermediate phenotype (n = 14–19, 8–12 weeks old). (**d**) The *Otp-Cre* conditional knockout males were more aggressive in the resident-intruder test than controls, showing more and longer attacks toward a male intruder (n = 9–11, 8–12

weeks old). (**e**) Gene set enrichment analysis of differentially expressed genes between *Otp-Cre; Cic*$^{flox/flox}$*; ROSA*^{fsTRAP} and *Otp-Cre; ROSA*^{fsTRAP} neurons. Data are represented as mean ± s.e.m. in **c**. All other data are presented in box-and-whisker plots, with center lines represent median, box limits represent interquartile range, and whiskers represent minimum to maximum data range. *: $P < 0.05$; **: $P < 0.01$; ***: $P < 0.001$; ****: $P < 0.0001$

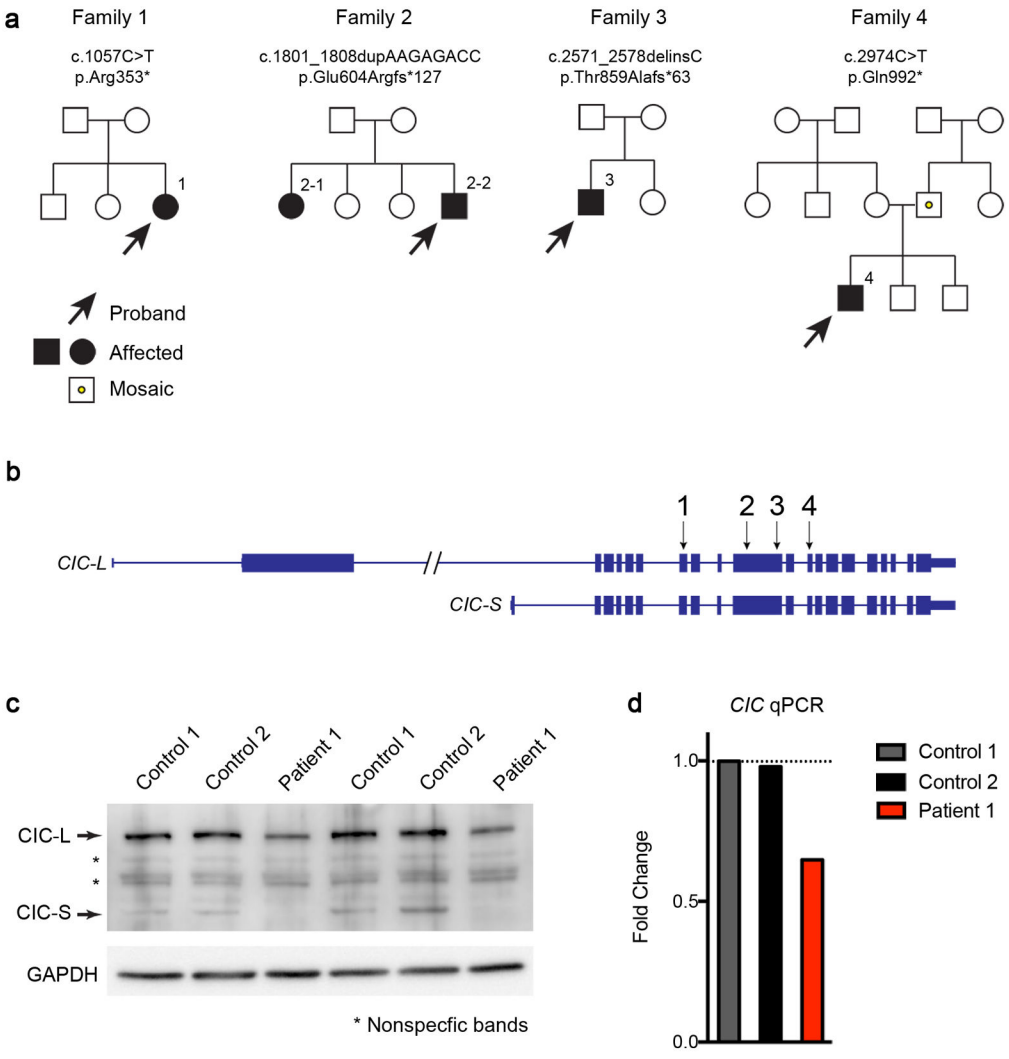

Figure 6. Identification of heterozygous *CIC* truncating mutations in four families

(**a**) Pedigrees of four families with *CIC* truncating mutations. Both patients in the second family have the same mutation, but neither parent harbors the mutation in their somatic DNA; one of the parents is presumed to be germline mosaic. Sanger sequencing of the *CIC* variant regions in the two unaffected siblings revealed they do not carry the same mutations in *CIC*. The father in the fourth family is a low-grade somatic mosaic as demonstrated by Sanger sequencing. (**b**) Genomic locus of human *CIC* showing the location of the mutations found in the four families. All four mutations are predicted to create premature stop codons. (**c**) Western blot analysis of fibroblasts from patient 1 and two controls showing that CIC protein levels were reduced in the patient. Images were cropped for better presentation. (**d**) qPCR of *CIC* from patient 1 and control fibroblasts showed that the RNA levels of *CIC* were reduced in fibroblasts from the patient. The expression levels were normalized to control 1, and fold changes were plotted. Five to six technical repeats were performed for each sample.

Table 1

Characteristics of patients with *CIC* mutations.

	1	2-1	2-2	3	4
Age at latest evaluation (years)	16	27	9	4	15
Gender	Female	Female	Male	Male	Male
Nucleotide change (NM_015125.4)	c.1057C>T	c.1801_1808dupAAGAGACC		c.2571_2578delinsC	c.2974C>T
Amino acid change	p.Arg353*	p.Glu604Argfs*127		p.Thr859Alafs*63	p.Gln992*
Inheritance	*De novo*	*De novo* (presumed germline mosaicism)		*De novo*	Paternally inherited (father mosaic)
ASD/Autistic features	+	−	−	+	+
Attention-deficit/hyperactivity	−	−	+	−	+
DD/ID	+	+	+	+	+
Seizures	+	+	+	−	−
Dysmorphic features	−	−	−	−	−
Head circumference at latest exam (cm)	57.5	N/A	54	50.2	54
Head circumference at latest exam (percentile)	99th	N/A	90th	32nd	27th
Latest MRI results	Multiple punctate foci of T2 hyperintensity within the subcortical white matter.	Normal brain MRI.	Normal brain MRI.	Single punctate focus of T2 hyperintensity within the right frontal lobe white matter.	Several periventricular T2 hyperintensities in the white matter, more concentrated in the parieto-occipital region.
Neurological symptoms at last exam	Normal muscle tone; normal deep tendon reflexes; no dyskinesia; no ataxia.	Normal muscle tone; normal deep tendon reflexes; normal gait; no ataxia.	Truncal hypotonia; normal deep tendon reflexes; normal gait; no ataxia.	Mild diffuse hypotonia; normal reflexes; no dyskinesia; no ataxia.	Normal muscle tone; hyperreflexia; no pyramidal syndrome; no ataxia.
Other	ALL, diastasis recti, mild telangiectasia.	Pulmonary stenosis.	Heart murmur, mild cutis marmorata telangiectasia.		Marfanoid habitus, stereotypic movements.

ASD: autism spectrum disorder, DD: developmental delay, ID: intellectual disability, ALL: acute lymphoblastic leukemia, N/A: data not available.